Technical University of Denmark

DTU

Characterization and influence of deformation microstructure heterogeneity on recrystallization

Godfrey, A.; Mishin, Oleg; Yu, Tianbo

Published in:
I O P Conference Series: Materials Science and Engineering

Link to article, DOI:
[10.1088/1757-899X/89/1/012003](10.1088/1757-899X/89/1/012003)

Publication date:
2015

Document Version
Publisher's PDF, also known as Version of record

[Link back to DTU Orbit]

DTU Library
Technical Information Center of Denmark

Characterization and influence of deformation microstructure heterogeneity on recrystallization

Characterization and influence of deformation microstructure heterogeneity on recrystallization

A Godfrey[1], O V Mishin[2] and T Yu[2]

[1]Key Laboratory of Advanced Materials (MOE), School of Material Science and Engineering, Tsinghua University, Beijing 100084, P.R. China
[2]Danish-Chinese Center for Nanometals, Section for Materials Science and Advanced Characterization, Department of Wind Energy, Technical University of Denmark, 4000 Roskilde, Denmark

E-mail: awgodfrey@mail.tsinghua.edu.cn

Abstract. The microstructure resulting from plastic deformation of metals typically contains heterogeneity on several length scales. This is also true for samples deformed to large strains, where an important form of heterogeneity is in the variation in microstructural refinement by high angle boundaries. A methodology for quantifying this type of heterogeneity based on the identification of areas classified as low misorientation regions (LMRs) is described, and some parameters for quantification of both the extent and length scale of LMRs are presented. It is then shown how this approach can be used to investigate the early stages of recrystallization in samples deformed to large strains, by direct comparison of electron backscatter diffraction (EBSD) maps of the same area before and after annealing. Methods for estimation of the stored energy of deformation from EBSD data are also surveyed and the problems of each for quantification of the local variation in stored energy are discussed, where it is concluded that a method based on the summation of the contributions from individual boundary segments is considered to be the best suited at present for characterization of the local variation in stored energy on the scale of the dislocation boundary features.

1. Introduction

For many metals plastic deformation results in a process of microstructural subdivision on several length scales by the formation of dislocation boundaries [1-3]. This in turn leads to a refinement in the microstructural scale, which in some cases can extend down to the level of just a few nanometres [4,5]. A large number of studies have been carried out to investigate the evolution of deformation microstructure with increasing strain, and have resulted in the establishment of a well-defined framework to describe this process in terms of the types of dislocation boundaries formed, their spacing and misorientation angle, and their relationship to the underlying slip pattern [6-8].

An important characteristic of such deformation microstructures is the presence of heterogeneity, or local variation, in the microstructure. This heterogeneity can take several forms, over different length scales. For samples deformed from low to medium strains heterogeneity is present on the grain scale, as a result of the orientation dependence of the deformation microstructure [9,10]. Such an effect can in fact also be seen in samples deformed by rolling to large strains if the initial grain size is sufficiently large [11,12]. Inside individual grains heterogeneity can also exist in the form of micro-shear bands and localized glide bands [13-15], where such features are most commonly observed at medium to high strains. Sample scale heterogeneity can also be important, either in the form of

macroscopic shear banding [16-18] or due to the nature of the applied deformation (for example, the effect of friction and roll gap geometry during rolling [19], or dead zones during compression).

The importance of the deformation microstructure for understanding recrystallization during annealing of deformed metals is well accepted. It is also worth pointing out, however, the high sensitivity of recrystallization to local variations in the deformation microstructure. This is true both for nucleation, for example, deformation zones around hard inclusions [20,21] or localized glide bands [22] as locations for potential nuclei, but also for growth of recrystallizing grains, where it is now recognized that protrusions and retrusions can form along a migrating recrystallization interface as a response to local variations in the deformed microstructure, and that the resulting interface profile can directly affect the average migration velocity of the interface [23]. A clear example of this high sensitivity to local variations in the deformation microstructure can be seen in the recrystallization behaviour of aluminium single crystals of $\{112\}\langle111\rangle$ ("Copper") and $\{123\}\langle634\rangle$ ("S") orientations deformed to a strain of $\varepsilon = 1.5$ by channel-die compression. For both crystals the average misorientation angles and spacings of the dislocation boundaries in the deformed microstructure, and hence the stored energy of deformation, are very similar [24], but for the Copper orientation crystal recrystallization starts at a temperature of 200°C after just 2 minutes, whereas for the S orientation crystal recrystallization is only observed at a temperature of 300°C after 30 minutes of annealing [25].

These observations highlight the importance of characterization of the deformed microstructure, and therefore estimation of the stored energy, on a scale that can capture such local variations, whether for analysis of recrystallization behaviour, or for use as an input to models of recrystallization. At present the two choices available for collecting such microstructure-based data are transmission electron microscope (TEM) observations and electron backscatter diffraction (EBSD) in the scanning electron microscope. TEM studies have the advantage of high spatial resolution and good angular resolution in measurement of the deformation microstructure, but only allow relatively small areas to be investigated even when making use of semi-automated or automated methods for measurement of crystal orientations [26-27]. In contrast, EBSD offers the possibility to collect microstructural data over several length scales (from tens of nanometres to millimetres), allowing heterogeneity within a deformed microstructure to be more fully characterized. The standard EBSD technique does however suffer from a limited angular resolution, such that boundary misorientations of a less than a certain angle (typically $1.5 - 2.0°$ for deformed samples) cannot be reliably identified [28-30]. Some consequences of this limitation in angular resolution for estimation of stored energy of deformation are considered later in this work. First we give an example of the use of the EBSD technique to quantify both the extent and length scale of deformation microstructure heterogeneity in samples deformed to large plastic strains, and show how this can be used to analyze recrystallization of such samples.

2. Characterization of heterogeneity in refinement at large plastic strains

2.1. Extent of refinement by high angle boundaries
There has been much interest in recent years in deformation to large plastic strains (so-called severe plastic deformation) by techniques such as equal channel angle pressing/extrusion (ECAP/ECAE), high pressure torsion, accumulated roll-bonding and heavy cold-rolling [31-33]. It is often assumed that the microstructure is uniform after deformation to large plastic strains, and in some cases the motivation for the use of such techniques is given as the preparation of samples with an ultra-fine grain size. However, even in samples deformed to large plastic strains, heterogeneity in the microstructure is present in the form of significant local variations in the refinement by high angle boundaries (HABs).

An example is given in figure 1, showing an EBSD map of a sample of aluminium AA1050 (99.5% purity) with an initial grain size of 45 μm after deformation by 8 passes of ECAE route Bc (90° sequential rotations between each pass) using a conventional split die with a sharp 90° corner. Further details of the processing conditions can be found in [34]. Note that all EBSD data in this paper were collected using the Oxford Instruments HKL Technology Channel 5 system. Some evidence of

heterogeneity in the microstructure can be seen in figure 1(a), in which all boundary misorientations >2° are marked by black lines. This heterogeneity is more clearly seen though in figure 1(b), where HABs (misorientation angle >15°) are marked by thick black lines and low misorientation angles (between 2° and 15°) are marked by thin black lines. The map shows that in many places there are regions predominantly containing only low angle boundaries (LABs). Based on this characteristic, these have been termed low misorientation regions (LMRs).
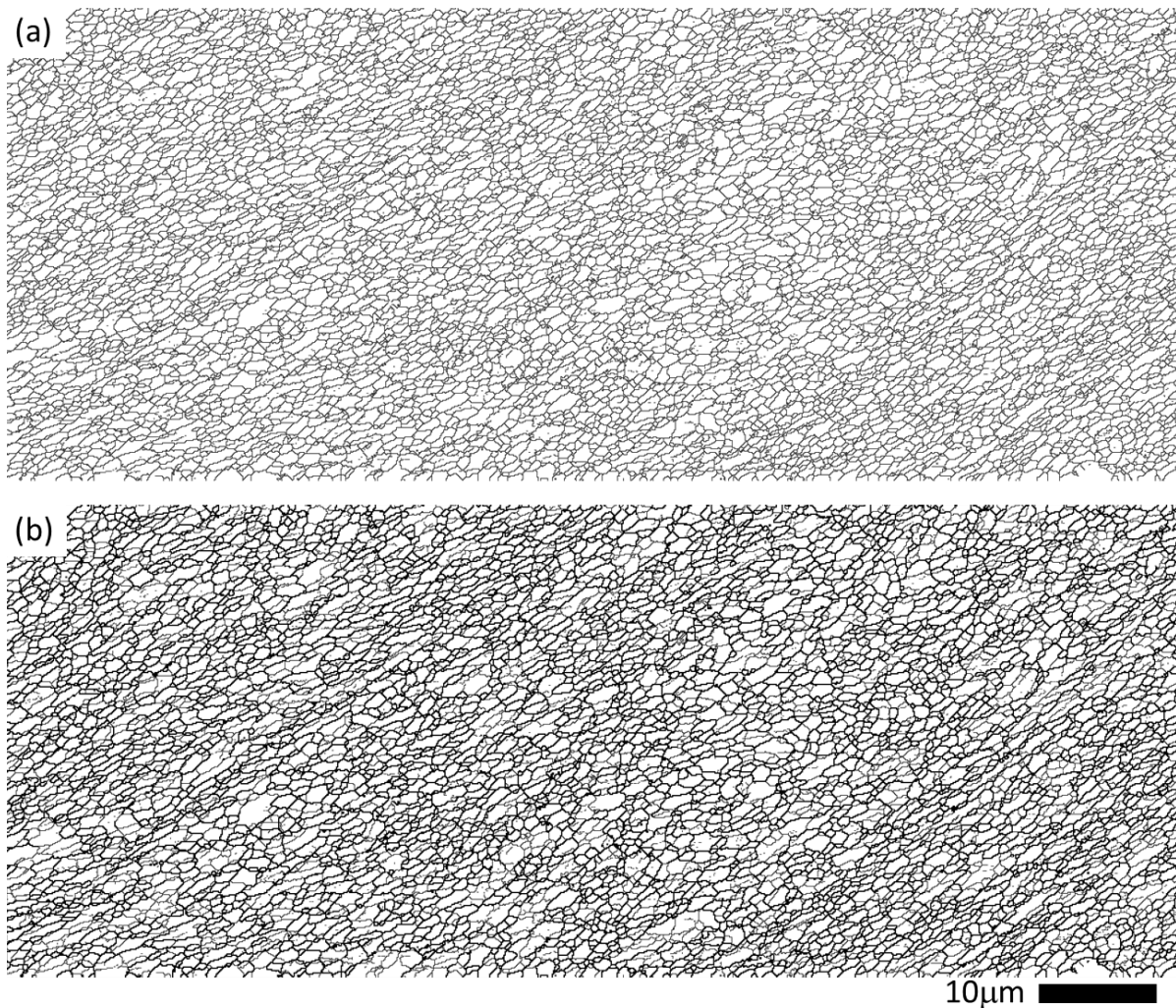

Figure 1. EBSD maps of ECAE-deformed aluminium AA1050 (8 passes; route Bc): a) all boundary misorientations > 2°; b) boundary misorientations >15º and 2° − 15° marked by thick and thin black lines, respectively.

A methodology to quantify the extent (volume or area fraction) of these LMRs using functions available in standard EBSD post-processing software has been proposed [35], as described in the following text. Firstly a "grain reconstruction" is performed using a misorientation angle definition of $\theta^G = 5°$. The result of such a procedure is shown in figure 2(a). Here each detected "grain" is coloured at random, and boundary misorientations of >5° and 2 − 5° are shown by thick and thin black lines, respectively. It can be seen that in some cases "grains" are detected, inside which no boundaries of lower misorientation angle are seen. In other cases, the detected "grains" contain boundaries of lower misorientation angle, and in many cases consist of clusters of dislocation cells. The use of quotation

marks here is, therefore, a reminder that the detected areas are not necessarily grains in a conventional sense, but are areas of the deformed microstructure bounded by misorientation angles of > 5°.

A subset of these "grains" with an area greater than a specified threshold value (A^*) can then be defined, as shown in figure 2(b) for $A^* = 2.5 \ \mu m^2$. The choice of this value for A^* is based on a multiple (10-times in this case) of d_{EBSD}^2, where d_{EBSD} is the average boundary spacing for the entire mapped area, measured via linear intercept measurement using the lowest appropriate misorientation threshold possible (typically 2° for such samples). In this way the LMRs identify places where the microstructure is predominantly subdivided by only <5° boundaries over a continuous area equivalent to at least 10 average-size dislocation cells/grains.
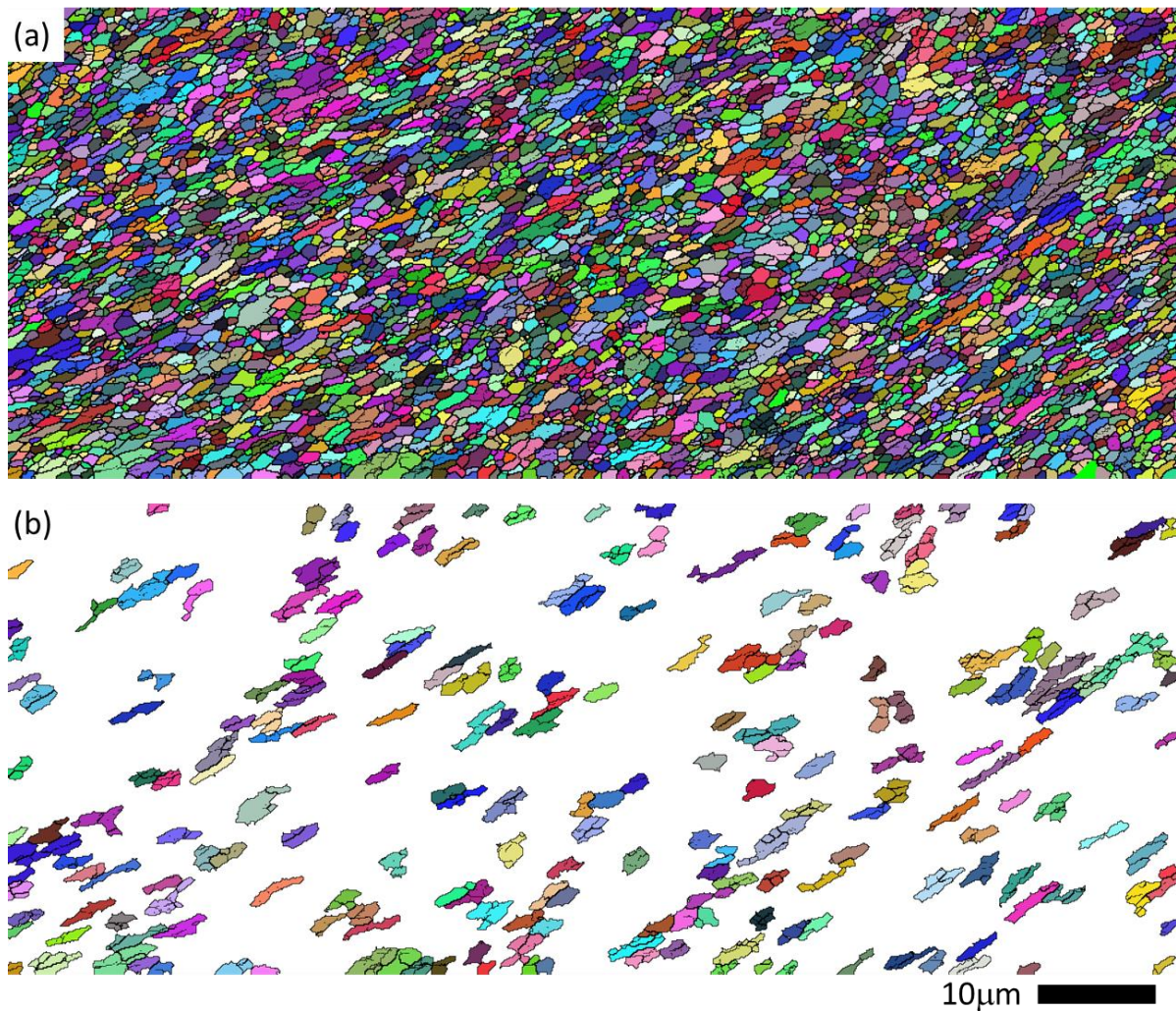
Figure 2. (a) EBSD map showing the result of applying a grain detection algorithm to the data shown in figure 1 using a grain boundary definition angle of 5°. The detected grains are coloured at random; (b) subset of the detected grains with size > 2.5 μm^2.

For samples deformed to large plastic strains the LMRs represent therefore locations of significant heterogeneity in the refinement by HABs. It is worth pointing out that the average boundary misorientation inside the LMRs is typically just a few degrees, such that if using the local microstructure as an estimate of the plastic strain, these regions would be regarded as deformed only to a rather low strain.

A quantitative measure of the extent of such heterogeneity is given by the area fraction of the mapped area covered by the LMRs, f_{LMR}. For the area shown in figure 2(b) $f_{LMR} = 19\%$, i.e. approximately 1/5 of this highly deformed sample has a microstructure corresponding to a significantly lower level of plastic deformation. It can be noted also that the LMRs are in some cases isolated but can also be found in clusters. In the latter case they may be separated by HABs, but nevertheless the microstructure in these areas is predominantly subdivided only by LABs. The remaining area of the map is, by default, designated as high misorientation regions (HMRs) – although in this case the HMRs in fact form a single percolating region. The value of f_{LMR} will of course depend on the choices of both A* and of the misorientation angle used for the initial "grain" detection (θ^G). A discussion of the motivations for the choices of the values for these parameters is given elsewhere [35]. The values used here have, however, been found to be good choices for comparing heterogeneity in refinement by HABs between samples deformed under a number of different processing conditions [34-41].
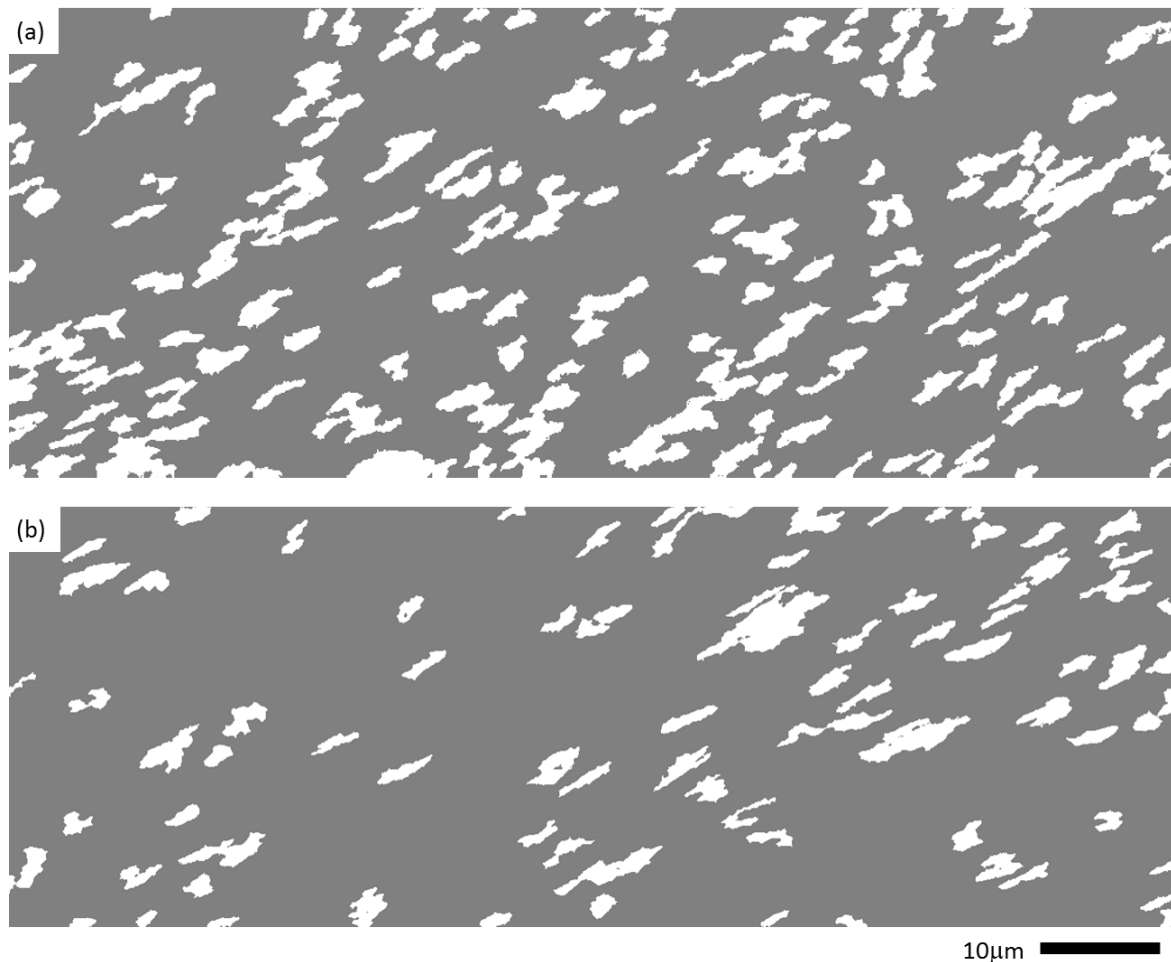
Figure 3. Phase-maps for two ECAE-deformed aluminium AA1050 samples showing LMRs in white, and the HMRs in grey: (a) sample described in [34]; (b) sample described in [40]. In each case $\theta^G = 5°$ and $A* = 10d_{EBSD}^2$.

Such a comparison is illustrated in figure 3, where LMR/HMR "phase maps" (showing the regions identified as LMRs in white and the remaining HMRs in grey) are given both for the ECAE-processed AA1050 sample described above, and also for another sample of the same material (AA1050) with a similar initial grain size (50 μm), deformed also by 8 passes via route Bc, but using a different 90°

ECAE die with a sliding floor [40]. It is evident that the extent of heterogeneity in refinement by HABs is lower for the latter sample, where f_{LMR} is calculated as 10%.

2.2. Estimation of length scale of heterogeneity

In addition to quantifying the extent of heterogeneity in refinement by HABs it is also of interest to determine the length scale of this heterogeneity. One obvious measure that is readily available is the average area of the LMRs, $<A>_{LMR}$. This parameter is influenced directly by the choice of $A*$, in that the area of any individual LMR by definition cannot be smaller than this value. Another perhaps obvious choice to quantify the length scale of heterogeneity would be average spacing between the LMRs. This, however, is difficult to measure in the standard way (e.g. measuring the distance between LMRs along randomly placed test lines) as the often highly convoluted nature of the LMR-HMR interface results in unreasonably low values for the LMR spacing [35].

An important observation to consider in designing a parameter to measure the length scale of the LMRs is the fact that, as seen in figure 2(b), the LMRs are frequently found in clusters. A schematic illustration of some extreme cases for different spatial distributions of LMRs is shown in figure 4. For each case the area fraction (f_{LMR}) is identical. In figure 4(a) the LMRs are non-clustered and randomly distributed, whereas in figure 4(b) they are also non-clustered, but are found in dense pockets. For the case of figure 4(c) the LMRs are strongly clustered, but the clusters can be regarded as being randomly distributed. Ideally any length scale measure should be able to distinguish between these different types of spatial distribution, as well as providing an estimate of the relevant length scale for each.
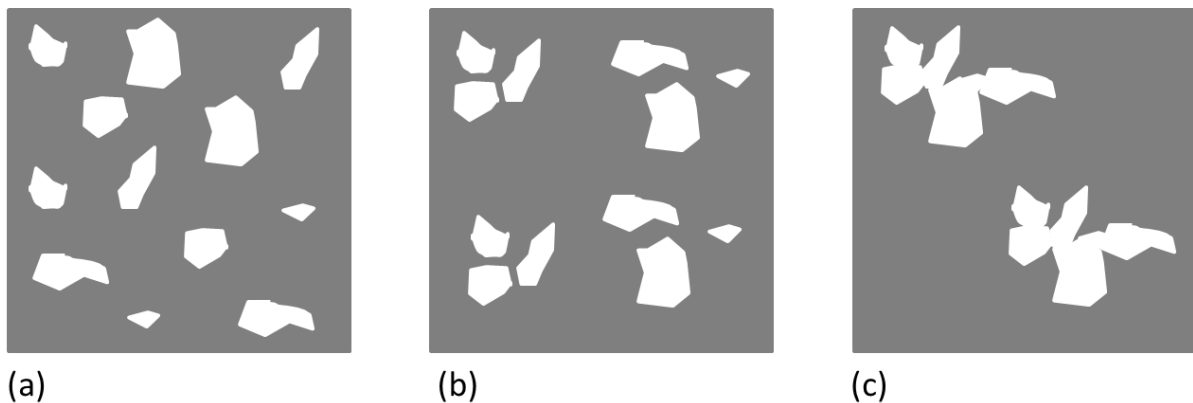

Figure 4. Schematic illustration showing some extreme cases for different spatial heterogeneity of LMRs: (a) non-clustered, random; (b) non-clustered, dense pockets; (c) clustered, with clusters randomly dispersed.

A simple parameter to estimate the extent of LMR clustering is the ratio of the average area of LMR clusters $<A_{LMR(cl)}>$ to the average area of the individual LMRs $<A_{LMR}>$. The difference between these two definitions is illustrated in figure 5, showing an enlarged view of a region of the EBSD map used in figures 1-3. In figure 5(a) each individual cluster is identified by a single colour, whereas in figure 5(b) each single colour identifies a LMR cluster. Note that not all LMRs are found in clusters; such LMRs are nevertheless included for the calculation of $<A_{LMR(cl)}>$, assuming in effect a cluster size of one. Values for the ratio of $R_A = <A_{LMR(cl)}>/<A_{LMR}>$ for the two data sets described previously are 2.1 and 1.3 for the ECAE samples deformed using a conventional split-die (hereafter Sample 1) and a sliding-floor die (Sample 2), respectively. More sophisticated measures can certainly be extracted, for example by considering the distribution of areas, but this simple measure already captures the smaller extent of LMR clustering in Sample 2.

As a measure of the length scale in the spatial distribution of the LMRs (and LMR clusters) a method has been proposed based on a statistical analysis of representative test areas of increasing size. The basic idea is to determine f_{LMR} as a function of map area, i.e., $f_{LMR}(A_{map})$ and use this data to

determine the minimum statistically representative area. For very small values of A_{map} (e.g. "maps" of area smaller than the average LMR area) a very large scatter in f_{LMR} will be found. As the value of A_{map} approaches the length scale of the heterogeneity, the scatter in f_{LMR} will decrease and approach a constant value. The idea is illustrated in figure 6, again using the data for Sample 1. As mentioned above, for the chosen θ^G and $A*$ the value of f_{LMR} for the entire map is 19%. If instead the map is divided into four sub-maps of 1/4 the map area, values of f_{LMR} = 18, 20, 22, and 23% are obtained. Similarly for eight sub-maps of 1/8 the map area, a still larger spread in f_{LMR} is obtained (in this case from 15% to 31%).
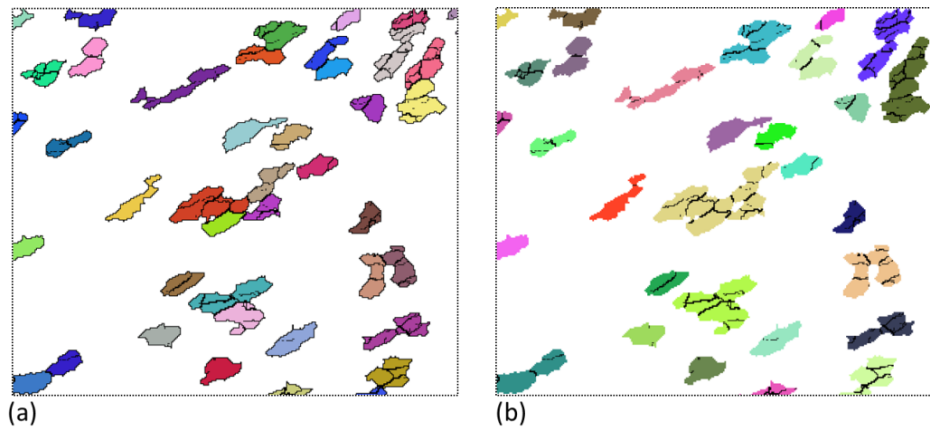

Figure 5. EBSD images, showing a subset of the map data for figures 1-3, illustrating the definition of individual LMRs and clusters of LMRs. In (a) each individual LMR is colored at random; in (b) LMR clusters are colored at random. Average areas are calculated based on the area of all coloured features.

In this case the original map in figure 3(a) has been divided into smaller non-overlapping areas (figure 6). In practice the calculation is best carried out by moving test-boxes of increasing area across a single large map, with some overlap between each test box, and then calculating the value of f_{LMR} for each position. Graphs showing the data following such an analysis of the EBSD maps of the ECAE-processed Sample 1 and Sample 2 are shown in figure 7, where the boxes were taken with a 50% overlap in both the x- and y-directions. As expected, for very small test box sizes the scatter in f_{LMR} is very large. With increasing test box size the spread in f_{LMR} decreases, and the values converge towards the average for the entire map area. An estimate for the length scale corresponding to the spatial distribution of the LMRs can then be obtained by determining the test box size where CV, the coefficient of variation (the relative standard deviation), falls below a pre-determined value. Here we use a value of $CV = 0.2$, giving representative test box lengths for the LMRs in Samples 1 and 2 of $L_{TestBox}$ = 15 μm and 25 μm, respectively. One requirement for such an approach is that the initial EBSD is large enough to fully capture the heterogeneity in the spatial distribution of the LMRs. With modern EBSD systems this is generally not a problem, but is something that should be remembered in planning a data collection strategy.

A summary of the comparison between the microstructural parameters for the two EBSD maps representing Samples 1 and 2 is given in Table 1. It is interesting to note that for both these samples the parameter most commonly used as a measure of the extent of microstructural refinement, namely the fraction of HABs (f_{HAB}), is almost identical. As such f_{HAB} does not provide any differentiation between the two microstructures, which is perhaps not surprising as this parameter does not contain any length scale information. The LMR-based parameters show that in addition to the smaller fraction of LMRs in Sample 2, the LMRs in this sample are of similar size, but significantly less clustered. The

larger value of L_{TB} for Sample 2 indicates however a larger mesoscale heterogeneity for this sample, which is supported by the visual impression from comparing figures 3(a) and 3(b).
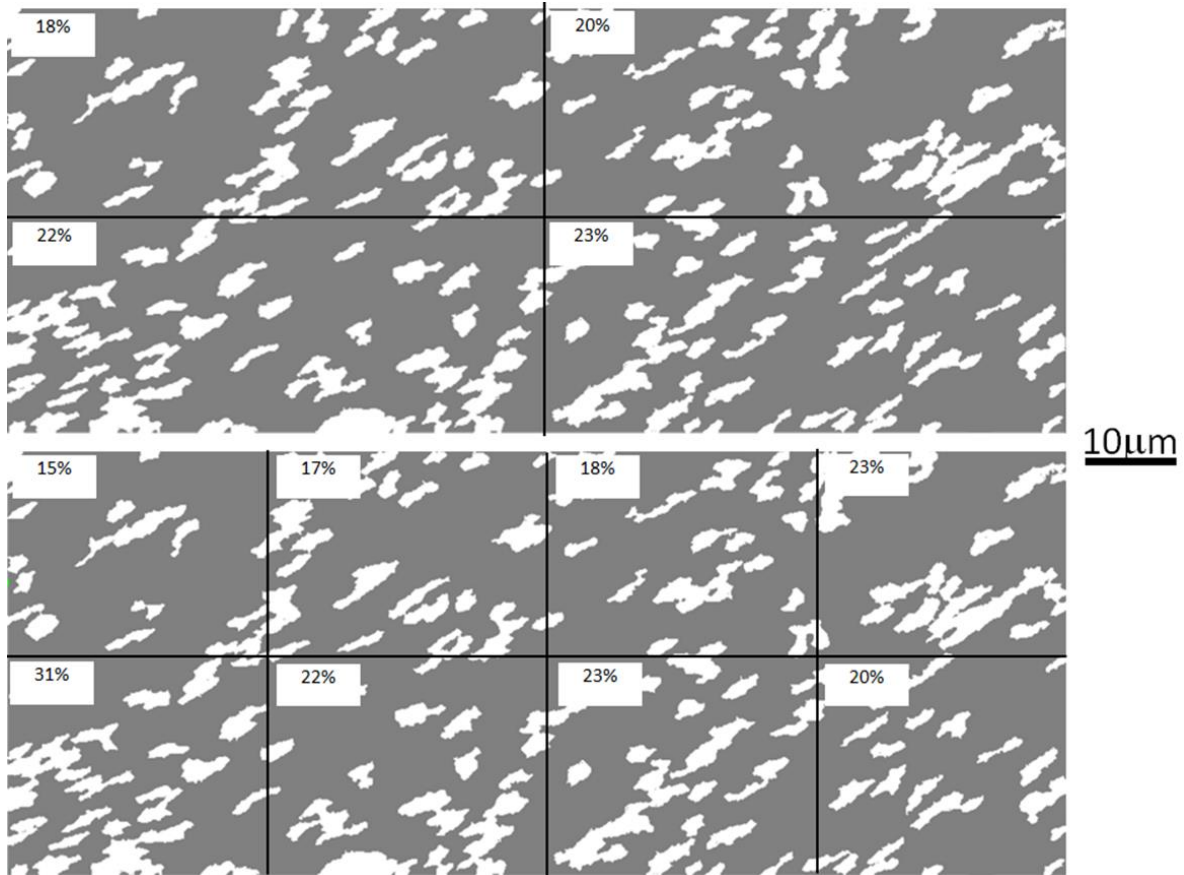
Figure 6. EBSD images illustrating length scale characterization by considering the variation in f_{LMR} with decreasing map area. The value of f_{LMR} for the entire map is 19%. Numbers in white boxes give the value of f_{LMR} for the sub-regions marked by black lines.
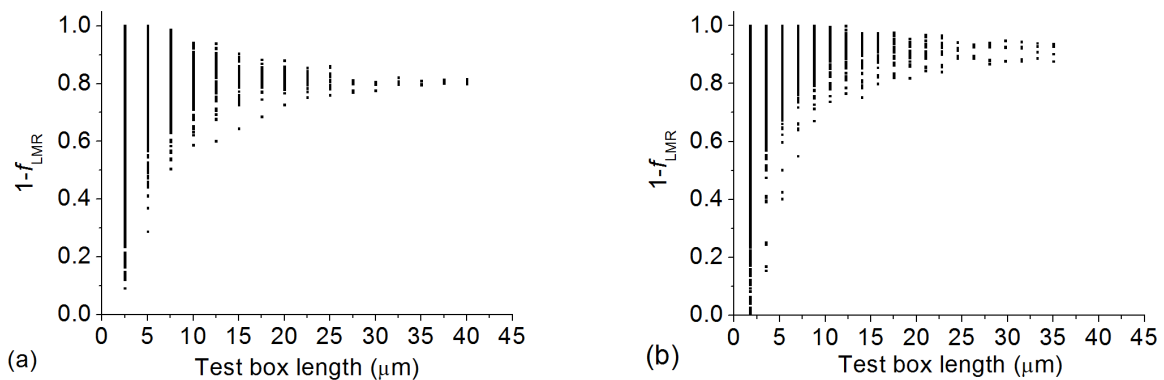
Figure 7. Variation of f_{LMR} (plotted as $1\text{-}f_{LMR}$) as function of increasing test-box size, calculated using test boxes with a 50% overlap: (a) Sample 1 - corresponding to data in figure 3(a); (b) Sample 2 - corresponding to data in figure 3(b).

Table 1. LMR characteristics for the EBSD maps representing two different ECAE-processed (8 passes via route Bc) samples of aluminium AA1050

Sample	f_{HAB}	f_{LMR}	$<A>_{LMR}$ (μm^2)	R_A (μm^2)	$L_{TestBox}$ (μm)
1	68%	19%	4.0	2.1	15
2	69%	10%	3.6	1.3	25

3. Influence of heterogeneity on recrystallization

The presence of heterogeneity in the form of regions of significantly different microstructural characteristics can be expected to have direct influence on the recrystallization behaviour of metals after deformation to large plastic strains. The annealing of such metals is of particular interest, as there exists some debate concerning how uniformly, or otherwise, microstructural coarsening takes place in such samples. Clearly, however, the presence of significant heterogeneity in the microstructure can be expected to have some influence on the annealing behaviour.

As an illustration of the relationship between nucleation of recrystallization and heterogeneity in refinement by HABs, an investigation of the annealing behaviour of a sample of copper, deformed by ECAE is presented here. The copper (99.98%) sample was deformed by 15 passes using route A (no rotation of the billet between ECAE passes) using a 120° die angle (further details can be found in [37]). The longitudinal section of this sample was polished mechanically followed by electropolishing. One region in this sample was mapped using EBSD first in the as-deformed state, and the same region was mapped again after annealing for 30 minutes at 160°C. This annealing treatment was chosen to yield material at the start of recrystallization. In order to allow a direct comparison between locations of the recrystallization nuclei and the deformation microstructure, the EBSD map after annealing was collected without mechanical re-polishing of the sample surface (the surface was only quickly electropolished to remove the oxide layer formed during annealing in air). The two maps were aligned using clearly recognizable features.

An EBSD map showing the examined region of the ECAE copper sample is given in figure 8(a), in which an inverse pole-figure (IPF) colouring is used. The microstructure is predominantly lamellar, as typical for ECAE samples processed using route A, and consists of bands of fine subgrains separated by bands of less refined material. This heterogeneity is highlighted in figure 8(b) where LMRs, identified using parameters of $\theta^G = 5°$ and $A^* = 10d_T^2$ ($= 2.1$ μm^2), are shown. For this map the LMR area fraction (f_{LMR}) is 32%. In this case the remainder of the map is formed of several large HMRs (in contrast to the cases shown above where the LMRs are distributed in a single fully connected HMR).

Figure 8(c) shows an IPF map of the same area after annealing at 160°C for 30 minutes. A number of small recrystallization nuclei are visible, both isolated and some found in clusters, confirming that the annealing treatment leads to an early stage of recrystallization. Figure 8(d) shows the locations of all the recrystallization nuclei in the mapped area. These were identified by first applying a grain detection procedure to the data set, and then using the average internal misorientation of each detected grain, as well as the size to identify a subset of the map containing the recrystallization nuclei. This automated procedure was able to pick-up most of the nuclei, though some minor manual adjustment of the subset was needed for cases where a nuclei retained some segment of low misorientation angle boundary to the adjacent deformed matrix.

Figure 8(e) shows the recrystallization nuclei superimposed onto the LMR/HMR phase-map for the as-deformed sample. Nuclei are seen predominantly in the HMRs, with 80% of the total nuclei area overlapping these regions and many nuclei fully inside HMRs. Very few nuclei are found fully inside LMRs. However, in several places nuclei overlap both LMR and HMR areas. In each of these cases the nuclei share a HAB with the adjacent LMR region. Although the LMRs represent regions of lower stored energy compared to HMRs, the fairly similar spread of orientations within the LMRs may provide good conditions for growth of recrystallization nuclei.

It should be remembered of course that there are always complications in interpretation of recrystallization mechanisms using only surface observations [42]. In the present case, however, the recrystallization nuclei are small and of comparable size to the LMRs and HMRs. As such even if the nuclei are formed below the sample surface, the location of the nuclei can still be related to the LMRs and HMRs. Nevertheless, it will be advantageous to use in-situ heating (to improve alignment between "before" and "after" data sets) and shorter annealing times (to confirm nucleation locations).
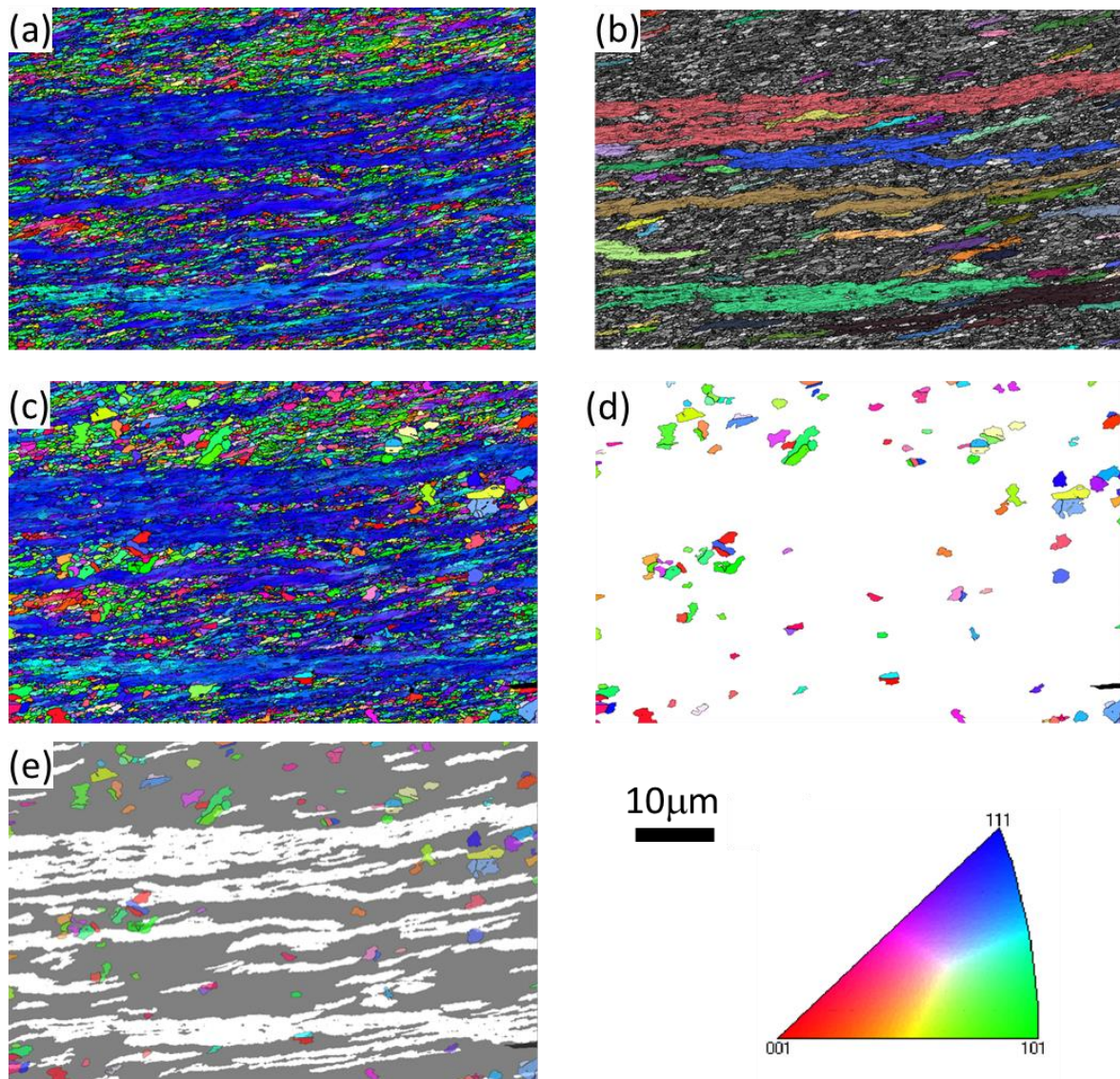
Figure 8. EBSD images of the same area of an ECAE-deformed copper sample before and after annealing at 160°C for 30 minutes: (a) before annealing (IPF colouring); (b) LMRs coloured at random and HMRs in grey; (c) after annealing (IPF colouring); (d) recrystallization nuclei; (e) recrystallization nuclei superposed on the LMR/HMR map of the as-deformed sample. For (a)-(d) thick and thin black lines represent misorientations of >15° and 2-15°, respectively.

4. Challenges in estimation of local stored energy

The stored energy of deformation provides the driving force for recrystallization, and is an important parameter for understanding both nucleation and growth of recrystallizing grains. In this regard the presence of heterogeneity in deformed microstructures requires the use of microstructure-based

measurements of stored energy, in order to capture important local variations. It is clear, for example, that the LMRs and HMRs presented above will have different local stored energy, but variations between the stored energy of individual LMRs may also be important. In the case of metals with medium-to-high stacking fault energies, such as nickel and aluminium, the majority of dislocations are arranged in the form of low-energy dislocation boundaries [1-8]. The stored energy, E_s, can therefore be expressed by the equation

$$E_s = \gamma S_V, \tag{1}$$

where S_V is the boundary area per unit volume, and γ is the energy per unit area of the boundary. Here the small contribution of loose dislocations between these boundaries is ignored. Detailed analysis [24,43] of stored energy may be carried out in the TEM based on equation (1) and stereology. However, such measurements are difficult and can only be made over relatively small areas. In contrast, the EBSD technique can provide quantitative microstructural data over large areas and has been used by a number of authors, e.g. [44-48], for estimation of the stored energy of deformation. It is important to remember, however, that the EBSD technique has limited angular and spatial resolution [49]. Care must therefore be taken when EBSD data are used for stored energy calculations, whether for examining local variations or for calculation of average values. In the following we describe some of the methods that have been proposed/used for estimating the stored energy of deformation from EBSD data sets, and then apply each of these methods to a data set collected from a sample of deformed nickel, with a view to highlighting some of the problems in making such local stored energy calculations. Note that in the following text for convenience we refer to any volume enclosed wholly or partly by dislocation boundaries as a subgrain, For accuracy, however, it should be remembered, however, that for dislocation cell-forming metals the term "subgrain" should be interpreted to mean "subgrain or dislocation cell".

4.1. Calculation methods based on EBSD data

4.1.1 The average method (Method A). The most straightforward method [45,46,50] for estimating the stored energy (E_s^A) is to calculate γ using the average misorientation angle θ_{av} based on the Read-Shockley equation and to take $S_V = \alpha/D_{av}$, where D_{av} is the average subgrain size and $\alpha = 3$ for equiaxed structures. A subgrain is taken as the smallest area fully surrounded by misorientation angles greater than the low cut-off misorientation angle (θ_{cut}) as shown in figure 9(a), and the equivalent circular diameter, d_{ECD}, [49] is then taken as the subgrain size. The average misorientation angle can be chosen in one of two ways: 1) $\theta_{H,av}$, the mean of misorientation angles above θ_{cut} (therefore considering the stored energy in all the boundaries); and 2) $\theta_{L,av}$, the mean of misorientation angles between θ_{cut} and 15° (considering only the deformation-induced LABs).

4.1.2 The modified average method (Method B). The modified average method is similar to the average method, using the average subgrain size and the average misorientation angle (which can again be chosen using either of the above two definitions). However, for this method only the misorientation angles along subgrain boundaries are considered in the calculation. In other words, the misorientation angles inside subgrains (dashed lines in figure 9(b)) are excluded in the calculation of the stored energy (E_s^B).

4.1.3 The segment method (Method C). In this method the stored energy (E_s^C) is calculated from each boundary segment in the EBSD map [44]. For each individual boundary segment (figure 9(c)), which is represented by the misorientation of two adjacent pixels, the boundary length per unit area is $L_{A,EBSD} = \Delta/A$, where Δ and A are the step size and the map area, respectively. In equiaxed structures, the boundary area per unit volume (S_V) and boundary length per unit area (L_A) have the relationship of $S_V = (4/\pi)L_A$. Additionally the stepped nature of EBSD maps requires a correction of $L_A = (\pi/4)L_{A,EBSD}$ [51]. Substituting these relationships into equation (1), the stored energy contribution from each boundary segment, $E_{s,i} = (\Delta/A)\gamma_i$, can be calculated, where the boundary energy γ_i is estimated from

the Read-Shockley function. The total stored energy over any examined area can then be determined as a sum of the contributions from all boundary segments as follows

$$E_s = \frac{\Delta}{A} \sum_i^N \gamma(\theta_i),$$ (2)

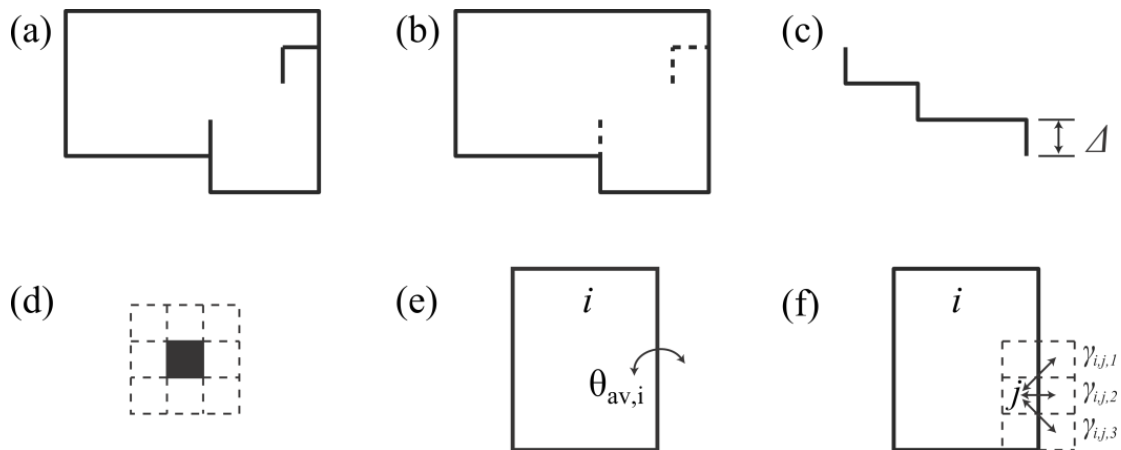where N is the total number of misorientation segments above θ_{cut}.

Figure 9. Illustration of methods for calculation of stored energy from EBSD data. (a) The average method includes all misorientation segments; (b) the modified average method excludes interior misorientation segments shown in dashed lines; (c) the segment method calculates the stored energy from each boundary segment; (d) the KAM method calculates the stored energy from each pixel; (e) the subgrain method performs boundary misorientation averaging for each subgrain; and (f) the modified subgrain method performs boundary energy averaging for each subgrain.

4.1.4 The kernel average misorientation (KAM) method (Method D). As an alternative to equation (1), the stored energy can also be expressed as the product of dislocation line energy (E_D) and the dislocation density (ρ) [52]

$$E_s = \rho E_D \approx \frac{\alpha \theta G b}{2d},$$ (3)

where G is the shear modulus, b is the Burgers vector, d is the boundary spacing, θ is the boundary misorientation, and α is a constant and 3 for mixed boundary type.

The KAM here is defined for a given pixel (figure 9(d)) as the average misorientation of that pixel with all its immediate neighbours, which is calculated with the proviso that misorientation angles above a high cut-off (5° or 15° as used [47,53]) are not counted in the averaging process, and misorientation angles below θ_{cut} are considered as zero degrees, but are still counted during averaging. This approach differs from other KAM definitions [47,53], where no low cut-off misorientation angle is used. If the boundary misorientation angle θ and the boundary spacing d in equation (3) are replaced by the average KAM value, θ_{KAM}, and the step size Δ, respectively, the stored energy (E_s^D) can be expressed in the following form

$$E_s = \frac{3Gb}{2\Delta} \theta_{KAM},$$ (4)

4.1.5 The subgrain method (Method E). After subgrain reconstruction with a certain value of θ_{cut}, the subgrain size D_i and the mean misorientation $\theta_{av,i}$ with its neighbours can be determined for each subgrain (figure 9(e)). Analogous to the average method, the stored energy associated with each subgrain can be obtained as

$$E_{s,i} = \alpha \frac{\gamma(\theta_{av,i})}{D_i} \qquad\qquad (5)$$

The average stored energy (E_s^E) of the entire measured area can then be estimated by using the average (weighted by area fraction) for all subgrains.

4.1.6 The modified subgrain method (Method F). This method is similar to the subgrain method; however, in the modified subgrain method the average boundary energy is calculated [48] instead of the average misorientation angle. For each subgrain, the boundary pixels are first selected, and then the misorientation angles of each of these pixels with its n neighbours (n ≤ 8 for a square-grid data set) on the other side of the boundary are converted into boundary energies based on the Read-Shockley equation. Figure 9(f) shows the situation for pixel *j* of subgrain *i*. The boundary energy of each subgrain can then be calculated using the following equation

$$\gamma_{av,i} = \frac{1}{N}\sum_{j=1}^{N}\left(\frac{1}{n}\sum_{k=1}^{n}\gamma_{i,j,k}\right), \qquad\qquad (6)$$

where N is the number of boundary pixels of subgrain *i*, and $\gamma_{av,i}$ is the average boundary energy of this subgrain. The area weighted average stored energy (E_s^F) can then be calculated by considering the whole map as for the subgrain method.
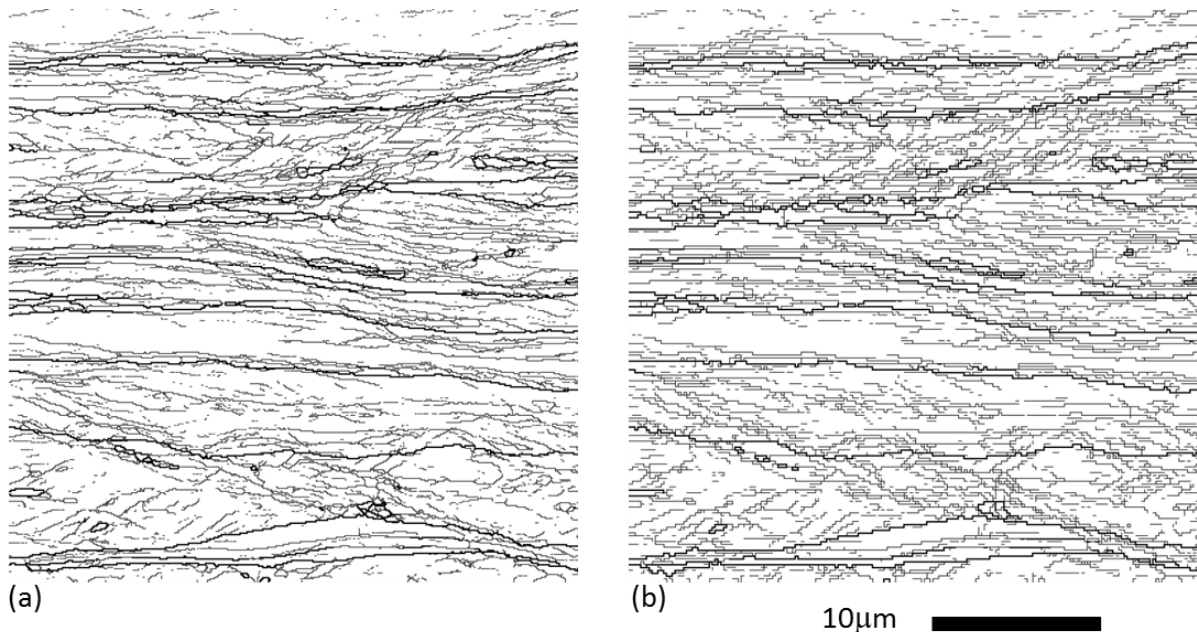

(a)   (b)

10μm

Figure 10. EBSD images of cold-rolled nickel for use in stored energy calculations: (a) experimental data at step size 0.05 μm; (b) resampled with a step size of 0.1 μm. Thick and thin black lines indicate misorientation angles of >15° and 2 – 15°, respectively.

4.2. Application to deformed nickel

High purity nickel (99.99%), cold-rolled to a thickness reduction of 90%, was examined using EBSD in the longitudinal section. A 400×400 pixel map, collected with a step size of 0.05 μm, was chosen for demonstration of the stored energy estimation. The average lamellar boundary spacing measured (θ_{cut} = 1.5°) in this map is 0.204 μm, which is very close to that measured from TEM images (0.21 μm) [54], and thus similar estimates of the stored energy (4.9 MJ m^{-3}) [43] should be expected. The effect of step size was investigated by artificially creating a 200×200 pixel map from the experimentally collected data set (effective map step size of 0.1 μm). For the stored energy calculations values of G = 79 GPa, and b = 0.249 nm were used.

The experimental EBSD data were first cleaned using the Channel 5 post-processing software. To further reduce the orientation noise, a maximum sub-grid minimum variance (MSMV) version of a modified Kuwahara filter [55] was applied to the data set. After data filtering, only a few interior misorientations were left. However, a large number of artificial single-pixel subgrains were still present along many LABs (see figure 10). The stored energy was then estimated for both maps using the methods described above, though it should be noted that single-pixel subgrains were excluded from the calculations involving subgrain reconstruction. The results are summarized in Table 2.

It is shown in Table 2 that both the step size and θ_{cut} affect the estimated stored energy significantly. A higher value of θ_{cut} results in a lower stored energy estimate for all methods examined, whereas the dependence of the stored energy estimate on the step size varies from method to method. For the average method and modified average method, the stored energy estimates (E_s^A and E_s^B) decrease with increasing step size, as larger mean ECDs are obtained with a larger step size. In contrast, for the segment method, the result (E_s^C) is almost independent of the step size used. Unexpected results were obtained for the subgrain method and the modified subgrain method, where the estimates (E_s^E and E_s^F) increase with increasing step size (discussed further in section 4.3.3).

The estimated stored energy is also affected by the choice of the average misorientation angle in the method A (the average method) and method B (the modified average method), with higher estimates obtained using $\theta_{H,av}$, and lower estimates using $\theta_{L,av}$. These two methods are very similar, but the latter ignores misorientation angles within subgrains, most of which are of very low misorientation angle, and thereby gives higher estimates than those calculated from the average method. Methods E and F (the subgrain method and the modified subgrain method) are grain-area weighted, and thus the results are strongly dependent on large subgrains, which are of low stored energy. Therefore much smaller estimates are obtained using these two methods.

Table 2. Stored energy (MJ m^{-3}) of cold rolled nickel estimated from experimentally measured EBSD data.

Step size	θ_{cut}	d_{ECD}	E_s^A		E_s^B		E_s^C	E_s^D		E_s^E	E_s^F
(μm)	(°)	(μm)	$\theta_{H,av}$	$\theta_{L,av}$	$\theta_{H,av}$	$\theta_{L,av}$		5°	15°		
0.05	1.5	0.33	7.1	4.9	7.8	5.7	3.5	3.6	7.5	1.9	1.4
0.05	2.0	0.41	6.5	4.7	6.8	5.6	3.0	2.8	6.7	1.3	1.0
0.10	1.5	0.38	6.1	4.2	6.4	4.5	3.4	3.9	7.5	2.9	2.0
0.10	2.0	0.46	5.4	3.8	5.7	4.3	3.0	3.2	6.8	1.9	1.4

4.3. Assumptions in the stored energy calculations and sensitivity to calculation parameters
In assessing the accuracy of the EBSD-based estimates of stored energy described above it should be remembered that the calculations all involve a number of important assumptions. A key assumption is that the majority of the energy left after deformation is stored in boundaries, whose energy can be described by the Read-Shockley equation. This is reasonable for metals with medium to high stacking fault energy, as both subgrain interior dislocations and extrinsic (redundant) dislocations within boundaries only contribute a small fraction to the stored energy [43,56]. However it should be still noted that this assumption results in underestimation of the stored energy as shown by comparison of DSC and TEM investigations [43]. A second common assumption is that subgrains in deformed metals are of equiaxed morphology. This assumption facilitates estimation, however, this will introduce some error in the results. A third key assumption is that θ_{cut} separates the misorientation angles of real boundaries from artefacts arising from orientation noise. This assumption, however, is only weakly satisfied due to the limited angular resolution of the EBSD technique, especially in highly deformed metals.

Some assumptions specific to particular stored energy calculations are also worth noting. For methods A and B the mean subgrain size and the mean misorientation angle are used. Therefore it is implicitly assumed that the subgrain size and the mean boundary misorientation angle have a narrow

distribution. In highly deformed metals, however, both the subgrain size and the boundary misorientation angle have a wide distribution due to structural heterogeneity, and thus the mean values cannot well represent the microstructure. For these methods there are two choices for the mean misorientation angle: (1) $\theta_{H,av}$, the mean of all detected misorientation angles, considering therefore stored energy in all boundaries; and (2) $\theta_{L,av}$, which only considers LABs and assumes that all the HABs (>15°) are initial grain boundaries. It follows that $\theta_{H,av}$ may be suitable at high strains and $\theta_{L,av}$ may be preferred at low strains, where there are few deformation induced high angle boundaries.

The KAM method is based on equation (3), which is derived from the idea that LABs are built up by dislocations. An implicit assumption in this method is that each pixel in the map can be regarded as a subgrain, whose misorientation angle with its neighbouring subgrains is represented by the KAM. This assumption may be reasonable when the EBSD step size is close to the real subgrain size, however in such a case the subgrain size will be estimated poorly. For fine step sizes the assumption is weak and lacks physical meaning. The use of a high cut-off misorientation angle, to eliminate the effect of initial grain boundaries, introduces another weakly supported assumption of this method, namely that the deformation induced dislocation boundaries all have misorientation angles below the chosen high cut-off misorientation angle.

4.3.1 Influence of the misorientation threshold. A low cut-off misorientation angle θ_{cut} is always required in estimation of stored energy from EBSD data due to the influence of orientation noise. It is clear therefore that this parameter plays a key role in the calculations, especially for regions containing many LABs (such as the LMRs in highly deformed samples) where orientation noise will have a larger effect. A suitable value of θ_{cut} should be chosen as a compromise of including as many real boundaries as possible, while introducing as few artefacts as possible.

The conventionally-used KAM method does not include a low cut-off misorientation angle [47,53], and as a consequence orientation noise can strongly influence estimated stored energy values. In the calculations described above a θ_{cut} is introduced into the calculation such that misorientation angles within the pixel kernel below this value are taken as zero degrees in calculating the KAM. This gives an improvement in the stored energy estimates, although the values still depend strongly on the choice of the high cut-off misorientation angle. For an EBSD map with step size Δ, map area A, total boundary length L, and mean boundary misorientation θ, approximately $2L/\Delta$ pixels will lie along subgrain boundaries. Furthermore, assuming a square-grid map, the mean KAM of these boundary pixels is approximately $3\theta/8$, since there are on average approximately three neighbours for all boundary pixels of a given grain, and the KAM of interior pixels is by definition zero degrees. Therefore, the global mean KAM is given by

$$\theta_{KAM} = \frac{(2L/\Delta)}{(A/\Delta^2)}\frac{3\theta}{8} = \frac{3}{4}L_A\theta\Delta \tag{7}$$

Combining this equation with the stereological relationship $(1/d) = (2/\pi)L_A$ (for an equiaxed structure) and inserting into equation (4) gives the following formulation of stored energy:

$$E_s = \frac{3Gb\theta}{2d}\frac{3\pi}{8} \tag{8}$$

This has the same form as equation (3), but with an additional coefficient of $3\pi/8$. This explains why the KAM method gives reasonable estimates in some cases despite its various limitations. It should be recalled also, however, that equation (3) assumes that the energy of subgrain boundaries increases linearly with misorientation angle, which according to the Read-Shockley function for boundary energy is only true for boundaries of very low misorientation angles (where the effects of orientation noise will be the greatest).

4.3.2 Subgrain reconstruction. In contrast to grain reconstruction in fully recrystallized samples, subgrain reconstruction in deformed samples is challenging, due both to the smaller structural scale and more importantly to the lower misorientation angles of many of the boundaries. Subgrain

reconstruction for an EBSD map of a deformed sample using a reasonable value of θ_{cut} invariably results in the detection of some huge subgrains, as even a single missing segment of a real boundary (due to the effect of orientation noise) leads to bleeding between neighbouring subgrains. At the same time orientation noise can also result in a large number of artificial single-pixel subgrains. Orientation filtering of the data does help to reduce the influence of the orientation noise [57,58], but only to a limited extent.

The effect of orientation noise on accurate subgrain detection is exacerbated by the fact that an apparent gradual change of orientation is often found as the electron beam is moved across boundaries of very low misorientation angle [59]. Preliminary studies show that such artificial gradients are found for boundaries with misorientation angle less than approximately 4°. Further work to establish the origin and extent of such effects is currently underway. It is assumed at present though that such artificial gradients arise as a result of the limited ability of the standard automated indexing procedures to distinguish overlapping EBSD patterns from volumes with very similar orientation. For these reasons it is clear that standard reconstruction of subgrains from EBSD data using low values of θ_{cut} based directly on orientation data is likely to be unreliable. Improvements may be possible by utilizing the observation of small cumulative misorientations either in pattern detection or for boundary detection, or alternatively by combining the orientation data with the pattern quality data [60], which has been shown in some cases to reveal clearly boundaries of low misorientation angle.

4.3.3 The step size. In order to correctly estimate the average subgrain size, a step size of less than 1/5 of the average subgrain size is required [49]. A larger step size gives larger mean values of d_{ECD} (Table 2), resulting in smaller estimates of the stored energy for the methods A and B (the average method and the modified average method). However, contrary to expectations, a smaller estimate of the stored energy is obtained for the smaller step size for the methods E and F (the subgrain method and the modified subgrain method). Closer examination of the data reveal that smaller step sizes give an increase in the size and number of very large subgrains for this data set as a result of the artificial changes in orientation measured across very low angle boundaries described above. The finer step size results therefore in a smoother artificial change in orientation, making it even harder to detect accurately boundaries of very low misorientation angle. This observation is a reminder that for the case of EBSD data, the presence of orientation noise means that a smaller step size is not always better, and that an appropriate step size (ideally close to 1/5 of the average size) should be chosen to estimate accurately the stored energy of deformation.

The data in Table 2 suggest that the segment method is not sensitive to the step size in the examined range. However, this method is also affected by any artificial gradual changes in orientation near very low angle boundaries. For example if a boundary of $\theta = 2°$ is detected as two boundaries of $\theta = 1°$, then the stored energy will be overestimated by approximately 20% according to equation (2). However, if θ falls below θ_{cut} there will be no contribution to the stored energy. The latter has a larger influence on the data in Table 2, as θ_{cut} is relatively high and the stored energy is underestimated compared to the TEM-determined value. In order to obtain the same stored energy of 4.9 MJ m^{-3} [43] as determined from TEM investigations, θ_{cut} has to be as low as 0.35° for the MSMV-filtered map with step size 50 nm. For the segment method therefore the lowest acceptable value of θ_{cut} without obviously introducing artificial misorientations within subgrains should be used for estimation of the stored energy.

4.4. Local estimates of stored energy
The various estimates of stored energy given above are illustrated based on application to a complete EBSD map, i.e. yielding an average value of stored energy for the entire map. Each of these can also be applied to smaller areas to obtain a more local variation in stored energy, and in each case will be subject to all of the same limitations in accuracy described above. In addition, however, there are some specific considerations that should be taken into account for the calculation of stored energy on a local

microstructural scale using these measures, particularly with regard to the length scale over which values can be calculated.

Methods A and B rely on the calculation of stored energy as an average over a number of subgrains, and as such these methods are not suitable for providing an estimate of stored energy on the scale of individual features in a deformed microstructure, although they may be used to estimate the stored energy within regions such as the LMRs or localized glide bands if these are sufficiently large. Similarly the individual subgrain-based methods (methods E and F) are limited by definition to providing a value for the stored energy on the scale of each individual subgrain. In one sense this should not be regarded as a problem, because in dislocation-cell forming materials it can be assumed that the majority of the stored energy of deformation is located at the deformation-induced boundaries. As such, a value of the stored energy for an individual subgrain has a clear physical meaning as the average stored energy for all the boundaries enclosing the subgrain. A corresponding limitation, however, is that the stored energy is necessarily associated with the entire subgrain, so that on a map-pixel basis an energy is unrealistically associated with the interior of each subgrain. Such a method though can be useful for example for models of recrystallization where it is necessary to decide the location where nucleation of new grains may take place.

The two remaining methods for estimation of stored energy (the segment and KAM methods) both have the advantage of being able to give a value for local stored energy on the scale of individual map pixels, and therefore with a spatial resolution limited by the EBSD step size. The KAM-based estimate is an appealing parameter, not least in that it provides a value directly for each pixel of a map, and hence in a format that can be easily visualized as a map, or imported into a model. As noted in section 4.3 previously, however, there are some problems with the way this parameter is calculated, particularly in that an average value is calculated for each pixel based on the misorientation to all the neighbour pixels within the kernel, typically including pixels that are not in fact separated from the kernel-centre pixel by real boundaries.

In contrast, the segment method has the advantage for quantification of local variations in stored energy in that the contributions from individual boundaries, which are assumed to exist wherever a pixel-to-pixel misorientation is larger than a pre-defined lower misorientation angle threshold (required to limit the influence from orientation noise in the EBSD data), are counted directly. The main disadvantage of this method stems from the fact that the stored energy is necessarily evaluated *between* map pixels and as such the result for a map of M x N pixels cannot be mapped directly on a pixel grid of similar size. One simple solution, however, to this is to calculate the stored energy based on a resampled grid where the new pixels are centred on the gridlines of the original map. Accordingly it can be concluded that the segment method should be the preferred choice for evaluation of the local variation in stored energy using EBSD data on the scale of the map step size.

5. Summary

Heterogeneity is a general characteristic of the microstructure of metals deformed over a wide range of plastic strains. For samples deformed to large strains a key heterogeneity is in the refinement of the microstructure by high angle boundaries, where even in samples deformed to very large strains a significant volume fraction of material can have a microstructure where locally the boundaries are predominantly only of low misorientation angle. This heterogeneity can be quantified by partitioning the microstructure into low misorientation regions (LMRs) and high misorientation regions (HMRs). The extent of such heterogeneity can be described by the area fraction of the LMRs (f_{LMR}), and a combination of parameters can be used to quantify the length scale of the LMR heterogeneity.

A detailed characterization of deformation microstructure heterogeneity is particularly important for studies of recrystallization, as this process can depend strongly on local variations in the deformed microstructure, and hence stored energy. For this purpose the EBSD technique has a strong advantage over other microstructural-based techniques in that it allows characterization over a wide range of length scale. Several methods have been proposed for estimation of stored energy from EBSD data. All of these methods are, however, sensitive to a lesser or greater extent to the limited angular

resolution of the EBSD technique, reflecting the fact that even after a large deformation many boundaries of low angle are still present. It can be noted that even the most accurate microstructure-based stored energy estimates (i.e. from TEM inspections) typically give values lower than found from differential scanning calorimetry (DSC) methods [43,56]. The reason for this difference is still not understood, but may relate to the energy of triple lines and/or the assumptions over the relationship between misorientation angle and boundary energy [56].

In any case the relative local variation in stored energy is important, and of the EBSD methods available, estimation of the stored energy by a summation of the contributions from individual boundary segments is considered to be the best suited at present for characterization of the local variation in stored energy on the scale of the dislocation boundary features. Given the advantage of the EBSD technique for collecting data over large areas with relatively high spatial resolution, the accuracy with which local variations need to be characterized (as limited by the angular resolution of the EBSD technique) is an important question. Improvements in angular resolution through new approaches to EBSD pattern analysis [61,62] may be possible, though the extent to which these methods can be used on samples deformed even to moderate strains is still not known. Similarly, although X-ray synchrotron measurements may in the near-future allow mapping of deformed microstructures with as low as 100nm resolution and an angular resolution of a fraction of a degree [63], only small volumes can be mapped with such a method. Here it is possible that models that capture the effect of stored energy variations on recrystallization can also help to provide guidance on the sensitivity to relative variations in stored energy, and hence the requirements for the accuracy in experimental characterization.

Acknowledgements

References

[1]   Hansen N and Kuhlmann-Wilsdorf D 1981 *Mater. Sci. Eng.* A **81** 141
[2]   Hansen N 2001 *Metall. Mater. Trans. A* **32** 2917
[3]   Hansen N and Juul Jensen D 2011 *Mater. Sci. Technol.* **27** 1229
[4]   Godfrey A and Hughes D A 2004 *Scr. Mater.* **51** 831
[5]   Hughes D A and Hansen N 2014 *Phys. Rev. Lett.* **112** 135504
[6]   Huang X and Winther G 2007 *Philos. Mag.* **83** 5189
[7]   Winther G and Huang X 2007 *Philos. Mag.* **83** 5215
[8]   Le G M, Godfrey A, Hong C, Huang X and Winther G 2012 *Scr. Mater.* **66** 359
[9]   Wert J A, Liu Q and Hansen N 1995 *Acta Metall. Mater.* **43** 4153
[10]   Huang X and Hansen N 1997 *Scr. Mater.* **37** 1
[11]   Chen H S, Godfrey A, Hansen N, Xie J X and Liu Q 2008, *Mater. Sci. Eng. A* **483-484** 157
[12]   Xing Q, Huang X and Hansen N 2006 *Metall. Mater. Trans. A* **37** 1311
[13]   Godfrey A, Juul Jensen D and Hansen N 1998 *Acta Mater.* **46** 835
[14]   Hughes D A and Hansen N 1993 *Metall. Trans. A* **24** 2021
[15]   Cizek P, Whiteman J A, Rainforth W M and Beynon J H 2004 *J. Microsc.* **213** 285
[16]   Duggan B J, Hatherly M, Hutchinson W B and Wakefield P T 1978 *Metal Sci.* **12** 343**.**
[17]   Jia N, Eisenlohr P, Roters F, Raabe D and Zhao X 2012 *Acta Mater.* **60** 3415
[18]   Armstrong R W and Walley S M 2008 *Int. Mater. Rev.* **53** 105
[19]   Mishin O V, Bay B, Winther G and Juul Jensen D 2004 *Acta Mater.* **52** 5761
[20]   Zhang Y H, Juul Jensen D, Zhang Y B, Lin F X, Zhang Z and Liu Q 2012 *Scr. Mater.* **67** 320
[21]   Xu W, Ferry M, Cairney J M and Humphreys FJ 2007 *Acta Mater.* **55** 5157
[22]   Paul H, Driver J H and Jasieńska Z 2002 *Acta Mater.* **50** 815
[23]   Moelans N, Godfrey A, Zhang Y and Juul Jensen D 2013 *Phys. Rev. B* **88** 054103

[24] Godfrey A, Hansen N and Juul Jensen D 2007 *Metall. Mater. Trans. A* **38** 2329
[25] Godfrey A, Juul Jensen D and Hansen N 2001 *Acta Mater.* **49** 2429
[26] Liu Q 1995 *Ultramicrosc.* **60** 81
[27] Liu Q, Huang X and Yao M 1992 *Ultramicrosc.* **41** 317
[28] Godfrey A, Wu G L and Liu Q 2002 *Mater. Sci. Forum* **408-412** 221
[29] Godfrey A, Mishin O V and Liu Q 2006 *Mater. Sci. Technol.* **22** 1263
[30] Mishin O V, Godfrey A and Juul Jensen D, Analysis of deformation structures in FCC materials using EBSD and TEM techniques *Electron Backscatter Diffraction in Materials Science* ed A J Schwartz et al (New York: Springer Science+Business Media) chapter 19 p263
[31] Segal V M 1995 *Mater. Sci. Eng. A* **197** 157
[32] Tsuji N, Ito Y, Saito Y and Minamino Y 2002 *Scr. Mater.* **46** 893
[33] Mishin O V, Godfrey A, Juul Jensen D and Hansen N 2013 *Acta Mater.* **61** 5354
[34] Mishin O V, Bowen J R and Lathabai S 2010 *Scr. Mater.* **63** 20
[35] Godfrey A, Mishin O V, Bowen J and Liu Q 2009 *Proc. 30th Risø International Symposium on Materials Science* ed J C Grivel et al. (Roskilde: Risø-DTU) p 31
[36] Mishin O V and Godfrey A 2008 *Metall. Mater. Trans. A* **39** 2923
[37] Mishin O V and Bowen J R 2009 *Metall. Mater. Trans. A* **40** 1684
[38] Luo Z P, Mishin O V, Zhang Y B, Zhang H W and Lu K 2010 *Scr. Mater.* **66** 335
[39] Mishin O V, Bowen J R and Godfrey A 2012 *Mater. Sci. Forum* **715-716** 825
[40] Mishin O V, Segal V M and Ferrasse S 2012 *Metall. Mater. Trans. A* **43** 4767
[41] Zhang Y B, Mishin O V and Godfrey A 2014 *J. Mater. Sci.* **49** 287
[42] Zhang Y B, Juul Jensen D and Godfrey A 2014 *Metall. Mater. Trans. A* **45** 2899
[43] Knudsen T, Cao W Q, Godfrey A, Liu Q and Hansen N 2008 *Metall. Mater. Trans. A* **39** 430
[44] Godfrey A, Cao W Q, Hansen N and Liu Q 2005 *Metall. Mater. Trans. A* **36** 2371
[45] Taheri M, Weiland H and Rollett A 2006 *Metall. Mater. Trans. A* **37** 19
[46] Choi S H and Jin Y S 2004 *Mater. Sci. Eng. A* **371** 149
[47] Takayama Y and Szpunar J A 2005 *Mater. Trans.* **45** 2316
[48] Lee K, Reis A C C, Kim G and Kestens L 2005 *J. Appl. Crystallogr.* **38** 668
[49] Humphreys F J 1999 *J. Microsc.* **195** 170
[50] Choi SH and Cho J H 2005 *Mater. Sci. Eng. A* **405** 86
[51] Cao W Q, Godfrey A and Liu Q 2003 *Mater. Sci. Eng. A* **361** 9
[52] Liu Q, Juul Jensen D and Hansen N 1998 *Acta Mater.* **46** 5819
[53] Kobayashi M, Takayama Y and Kato H 2004 *Mater. Trans.* **45** 3247
[54] Hughes D A and Hansen N 2000 *Acta Mater.* **48** 2985
[55] Godfrey A 2004 *Scr. Mater* **50** 1097
[56] Godfrey A and Liu Q 2009 *Scr. Mater.* **60** 1050
[57] Mishin O V, Östensson L and Godfrey A 2006 *Metall. Mater. Trans. A* **37** 489
[58] Mishin O V and Godfrey A 2007 *Mater. Sci. Forum* **550** 295
[59] Bate P S, Knutsen R D, Brough I and Humphreys F J 2005 *J. Microsc.* **220** 36
[60] Barou F, Maurice C, Feppon J and Driver J 2009 *Int. J. Mater. Res.* **100** 516
[61] Wilkinson A J, Britton T B, Jiang J and Karamched P S 2014 *IOP Conf. Ser.: Mater. Sci. Eng.* **55** 012020
[62] Maurice C, Quey R, Fortunier R and Driver J H 2013 High Angular Resolution EBSD and Its Materials Applications *Microstructural Design of Advanced Engineering Materials* ed D A Molodov (Weinheim, Germany: Wiley-VCH Verlag GmbH & Co KGaA) chapter 14 p 341
[63] Ice G E et al. 2009 *Mater. Sci. Eng. A* **524** 3